Nanotribological investigation of sliding properties of transition metal dichalcogenide thin film coatings

Ales Rapuc,[†,] Kosta Simonovic,[‡] Teodor Huminiuc,[†] Albano Cavaleiro,[§] and Tomas Polcar[†,‡,*]*

†) Engineering Materials Group, Faculty of Engineering and Physical Sciences, University of Southampton, Southampton SO17 1BJ, United Kingdom

‡) Department of Control Engineering, Faculty of Electrical Engineering, Czech Technical University in Prague, Technicka 2, 16627 Prague 6, Czech Republic

§) SEG-CEMMPRE, Department of Mechanical Engineering, University of Coimbra, Rua Luís Reis Santos, 3030-788 Coimbra, Portugal

KEYWORDS

Atomic force microscopy, nanotribology, thin film coatings, solid lubrication, transition metal dichalcogenides, Raman mapping

ABSTRACT

Transition metal dichalcogenide (TMD) based coatings are known for their low friction performance, which is attributed to the formation of a tribolayer consisting almost exclusively of

pure well-ordered TMD. However, the formation of such a tribolayer and its wear track coverage is still unknown. In this study, we employed surface mapping and nanotribological techniques to study the properties of the wear tracks of composite W-S-C coatings. Our analysis revealed that the as-deposited coating consisted of two phases, with significantly different nano-scale frictional properties. We attributed the phases to nanocrystalline WS_2 (low friction) and amorphous solution of carbon and WS_2 (high friction). The two phases wear at different rates, especially at lower loads, where we observed faster depletion of nanocrystalline WS_2. In the wear track, sparse flat WS_2 flakes were identified, suggesting that the recrystallization of the WS_2 phase occurs only at the spots where the contact pressure is the highest.

1. INTRODUCTION

Modern engineering applications require sufficiently lubricated surfaces, to comply with the increasingly demanding performance and strict environmental regulations.[1] Despite great progress in the field of tribology, significant amounts of energy are lost globally due to friction and wear,[2] with estimations that up to 11% of energy in transportation can be saved by adequate advancements in understanding friction.[3] Furthermore, the increasing presence of man-made mechanical systems in space necessitates the use of highly developed technical materials. These systems operate in environments ranging from Earth to outer space and are therefore subjected to a wide range of operating conditions (i.e., temperature, humidity, pressure, radiation, etc.).[4] For example, the high vapor pressure of most liquid lubricants[5,6] limits their applicability in space applications; hence, alternatives have to be proposed. The two most researched replacements are solid lubricants[4,7] and ionic liquids.[5] While ionic liquids can provide sufficient tribological performance due to their low vapor pressure,[8] their main drawbacks are tribo-corrosion,[9] toxicity

to the environment,[10] rapid decomposition,[11] and limited temperature range.[11] On the other hand, most solid lubricants exhibit decreasing friction with increasing contact stress. Their lubricating properties mainly arise from a low shear transfer film between the surface material and the counter body, which is often formed by tribo-chemical reactions on the surface.[7] Consequently, the performance of solid lubricants is highly dependent on the working environment. Therefore, research in recent years has been focused on improving the tribological and mechanical properties of solid lubricants, with the aim of achieving favorable performance in a wider range of environments.[12–14]

There are two main approaches to achieve sufficient solid lubrication: (i) incorporation of solid lubricant within the bulk material,[15] or (ii) applying a solid lubricating film on one of the sliding bodies.[4,7] Powder metallurgy is the commonly used method for the incorporation of the lubricant in the bulk material.[15,16] The method provides large amounts of lubricant material[16] but usually produces uneven and discontinuous transfer film with poor adhesion.[4] On the other hand, physical vapor deposition (PVD) techniques, such as sputtering[17–19] or pulsed laser deposition,[12] are used for the application of thin coatings. The main distinction is that the coatings produce a thin, continuous and uniform tribo-film; however, they are limited by a relatively short component lifetime.[4]

There are four distinct groups of solid lubricants: (i) carbon-based materials, (ii) transition metal dichalcogenides (TMDs), (iii) polymers, and (iv) soft metals, and most of them can be applied in the form of thin coatings.[7] In this work, we will focus only on transition metal dichalcogenides, which have shown good lubricating properties in high and ultra-high vacuum environments.[4,6]

The unique lamellar structure of TMDs gives rise to their superior low-friction properties, where strong covalent bonding within the layers provides the required structural stability, while weak van der Waals interactions and large separation distances between the layers allow for easy sliding.[20] The most representative compounds from the group, MoS_2 and WS_2, have been successfully applied as thin films since the late 1960s[21,22] and early 1970s,[23] respectively. They provide the best tribological properties in vacuum or dry nitrogen environments, while humidity and oxygen in the atmosphere significantly increase friction and wear rates.[4,6,14] Furthermore, TMD thin films can suffer from low hardness and low adhesion to the substrate.[14] Coatings can be modified by alloying with metallic (Ti,[24] Cr,[25,26] Au,[26–28] Al,[27] Pb,[29] Ni,[26] and Co[26]) or non-metallic components (C,[13,19,30–33] and N[34–36]), which can mitigate the limited mechanical properties or the detrimental environmental effects.[14] In particular, doping with carbon to form nano-composite structured coatings (such as W-S-C,[30,31] Mo-Se-C,[13,19] Mo-S-C,[32] or W-Se-C[33]), can significantly improve hardness and wear resistance and allow self-adaptive behavior.[17,30] Similarly, nitrogen has also been successfully incorporated as a doping material to improve tribological performance of pure TMDs.[34–36]

Unlike macro-scale tribology, where the overall performance of the coatings is studied in the simulated operational conditions with a macroscopic tribometer in various configurations (i.e., ball-on-disc, pin-on-plate etc.),[37] nano-tribology deals with fundamental sliding properties and concerns contacts ranging from a few to hundreds of nanometers.[38] Atomic force microscope (AFM) probe mimics a single nano-scale asperity contact,[39] thus offering a possibility for a wide array of nano-tribological investigations. Friction force microscopy, which utilizes a measurement of lateral forces of the AFM probe in contact with the sample, has been previously

successfully employed to study nano- and atomic- scale tribological properties of 2D materials: graphite,[40] graphene,[41,42] exfoliated TMDs,[42,43] thin film TMD based coatings,[44–46] or h-BN[42].

In this work, we examine the multi-scale surface mapping approach to wear track analysis, combining different techniques, including optical profilometry, scanning electron microscopy (SEM), transmission electron microscopy (TEM), atomic force microscopy, and spectral Raman mapping to examine the characteristics of the wear tracks. Since single point analysis is, in most cases, insufficient to qualitatively distinguish localized effects in non-homogeneous systems, such as wear tracks, surface mapping provides a much broader and wholesome insight in the origins of friction. For example, TEM analysis is limited to analyzing only tens of nanometers at one time, and conventional micro-Raman analysis is usually limited to a number of single points with a diameter close to 1 micrometer.

We present a comprehensive study of the wear track properties, focused on nano-tribology techniques to analyze nano-scale frictional properties of TMD thin films. The use of Atomic Force Microscopy in contact mode, as opposed to other standard techniques for the analysis of wear tracks, such as Raman spectroscopy, electron microscopy and spectroscopy or X-Ray methods, allows us to specifically study the interface between the sliding body and the sample. Since the conventionally used methods employ some form of electro-magnetic (EM) radiation (visible light, X-rays) or electron beams to probe the sample, the resulting signal would always contain information from below the surface, which can mask the properties on the interface.[47] Additionally, the energy introduced in the system by the measurement procedure might induce changes in the crystal structure as well.[48] As a case study, we employ a composite W-S-C system to investigate how the nano-scale properties compare across different sections of the sample and correlate them with their frictional behavior on the macro-scale.

2. EXPERIMENTAL SECTION

2.1. Materials and deposition

The W-S-C films were deposited using a d.c. magnetron sputtering chamber (Teer, UK) on to polished WC discs. Prior to the coating deposition, the substrates were cleaned by establishing the plasma close to the substrate electrode for 30 minutes. Four targets were used: chromium (Cr, purity 99,9%), two graphite targets (C, purity 99.6%) and one WS_2 target (purity 99%). After plasma etching, the substrates were first coated by a thin bonding layer, consisting of pure Cr and of Cr with increasing amount of W-S-C at the interface, with the top layer deposited at a pressure of 0.3 Pa and an applied substrate bias of -50 V. Finally, the W-S-C layer was deposited at a pressure of 0.45 Pa (without bias) by using two graphite and one WS_2 target. The thickness of functional W-S-C coating with homogeneous composition was 1 micrometer.

2.2. Coating and wear track characterization

Chemical characterization of the as-deposited coatings was performed using Raman spectroscopy ($\lambda_{laser} = 532\,nm$; XPlora, Horiba Scientific, France), energy dispersive spectroscopy (EDS) and X-ray photoelectron spectroscopy (XPS; Thermo Scientific Theta Probe XPS, UK). Moreover, Raman spectroscopy was used to perform spectral Raman mapping of the wear tracks over a large area (50 x 10 μm). A total of 561 points per sample were recorded with a separate Raman spectrum obtained for each point. Raman maps were compiled by determining the local height of the corresponding WS_2, WO_3 and carbon peaks, at 408 cm^{-1} (A_{1g} mode), 798 cm^{-1} and 1568 cm^{-1} (G-peak) respectively. The average Raman spectra for each sample were obtained by averaging over all 561 measurements comprising the maps. The resulting spectra were then normalized to a comparable scale between the samples. The resolution of the Raman

signal was kept low (2 cm^{-1}), as we were mainly interested in the distribution of carbon and WS_2 across the wear tracks, rather than detailed convolution of the peaks.

After the macroscopic friction tests, a Zygo NV7200 (Zygo, United States) 3D white light optical profilometer was used to characterize the macroscopic wear patterns of the coatings. Eight points over the wear track were measured, and the results were averaged and reported as the total wear volume together with average width of the wear track for each load. The SEM imaging, as well as the focused ion beam (FIB) specimen preparation were performed using a FEI Helios Nanolab electron microscope. The high-resolution transmission electron microscopy (TEM) micrographs were acquired using an FEI Titan Themis Cubed operating at 300kV acceleration voltage and equipped with an image aberration corrector.

2.3. Macroscopic tribological test

Macroscopic tribological tests were performed in the unidirectional, rotational ball-on-disc configuration with the custom-built vacuum tribometer, VacTrib01 (Advanced Materials Group, Czech Republic). In total, four tests were performed at normal loads of 2, 8, 10, and 20 N, respectively. Each test was running for 5000 cycles at a linear speed of 5 cm/s. Steady-state coefficient of friction (μ_{macro}) was obtained as the average value of the friction coefficient from the last 30% of the test. Since the focus of this work is nano-tribological characterization, only the relevant results of the macro-scale tribo-tests are presented.

2.4. Nanotribology

Atomic force microscopy (Agilent 5500, USA) was used in contact mode to obtain topography, friction maps and to perform load-dependent friction measurements on the coatings

and the wear tracks. Topography and friction maps were obtained simultaneously by applying constant force during the measurement (*i.e.,* constant force mode).

Load-dependent friction measurements were performed by incrementally increasing contact load every 25 lines over the 250 x 250 nm area. A total of 10 different loads were applied, including negative loads, used to observe the behavior in the adhesive regime. Pull-off force $F_{pull\text{-}off}$ ($\approx F_{adh}$) was measured just before each friction experiment, and the minimum load F_{min} was selected accordingly. More precisely, the minimum load was determined empirically for each measurement, as the lowest load at which the tip would not lose contact with the surface during continuous sliding. The minimum and maximum loads applied during each measurement are summarized in Table 1. A custom script was utilized to precisely control the loads in the experiment. Sliding speed was kept constant at 1 ln/s.

Table 1. Nanotribology measurement parameters.

Scan region	F_{adh} (nN)	F_{min} (nN)	F_{max} (nN)
As-deposited – low friction	6.9	-4.1	30
As-deposited – high friction	7.5	-1.5	30
Wear track – low friction	10.9	-6.5	30
Wear track – high friction	12.1	-6.1	30

Nanosensors™ PPP-LFMR probes with nominal spring constant 0.2 N/m were used (NanoWorld AG, Switzerland). Actual normal spring constant (k = 0.19 N/m) was determined *in-situ* by a built-in thermal noise method.[49] Lateral forces were calibrated according to wedge

calibration procedure[50] using a commercial TGF11 (μMasch, Bulgaria) calibration grating. The obtained lateral calibration coefficient was $\alpha = 434\ nN/V$.

3. RESULTS

3.1. As-deposited coating characterization

The chemical composition of as-deposited coating was determined by EDS and is shown together with the hardness and elastic modulus in Table 2.

Table 2. Elemental composition of the as-deposited coating.

W (at%)	S (at%)	C (at%)	O (at%)	Hardness (GPa)	E_r (GPa)
18	35	40	7	7.6 ± 0.6	87 ± 4

Chemical bonding was evaluated by XPS. Note that the surface of the sample was cleaned by Ar ion bombardment, which preferentially sputter sulfur. Therefore, XPS can be used here only qualitatively. From the detailed analysis of the core-level spectra of S2p, C1s and W4f metallic tungsten was formed in addition to WS_2 and WC, as indicated by elemental composition, and spectra shift towards lower binding energies. Note that some traces of S−O, C−O, and C−C bonds were observed; the latter may indicate the presence of an amorphous carbon phase. A more detailed description of XPS results was given previously.[44]

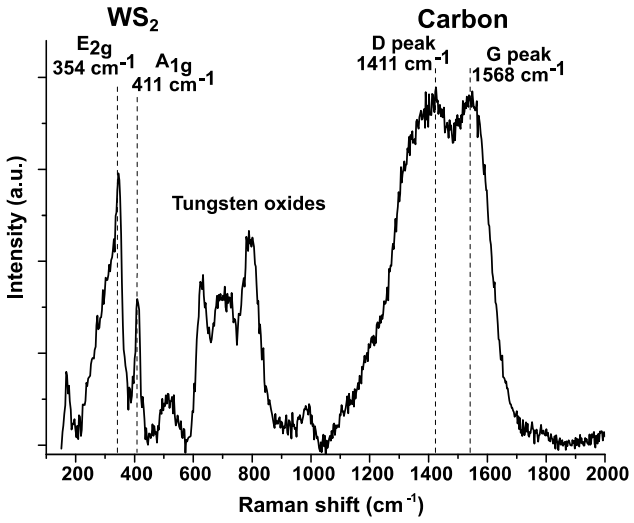

Figure 1. Raman spectrum of the as-deposited coating.

A Raman spectrum of the as-deposited coating is shown in Figure 1, and three distinct regions are identified. First, the carbon G and D peaks, representing different sp_2 hybridization, are located at 1568 cm^{-1} and 1411 cm^{-1}, respectively.[51] After the deconvolution of the spectra, intensity ratio of the two carbon peaks (I_D/I_G) was calculated as 2.05; according to the 3-stage model of the carbon structures presented by Ferrari et al.,[52] I_D/I_G ratio represents the amount of the sp_2 bonded carbon in the investigated material. Hence, according to the obtained value (I_D/I_G = 2.05) it follows that in the as-deposited coating, the carbon matrix was nanocrystalline with more than 80 % of the sp_2 bonding structure composed from aromatic clusters with long ordered C-C chains.[52] Secondly, two main peaks of the WS_2 structure[53] were identified (Figure 1); A_{1g} peak at 411 cm^{-1} and E_{2g} peak at 354 cm^{-1}. After the deconvolution, intensity ratio ($I_{A_{1g}}/I_{E_{1g}}$) was calculated to 0.88, thus, the shear vibration mode of the WS_2 structure is dominant.[54] Moreover, the lower intensity of the A_{1g} peak indicates a low number of the WS_2 monolayers on the surface of the virgin coating.[55] Finally, in the range between 500 and 1000 cm^{-1} oxides of tungsten (WO_x) were identified as a consequence of the WS_2 oxidation.[25,56]

3.2. Macroscopic tribo-tests

The coefficient of friction for investigated loads, together with the wear volume and wear track width, are presented in Table 3. The coefficient of friction decreases initially with the increase of normal load (from 2 N to 8 N) and increases afterward for higher loads (10 N and 20 N). The wear, on the other hand, does not follow the same behavior. Namely, wear volume remains constant until the sharp increase at 20 N load, while the wear track width increases steadily with the increase of load.

Table 3. A summary of the relevant macro-tribology results.

Load (N)	μ_{macro} (/)	Wear volume (mm^3)	Wear track width (mm)
2	0.039	0.9	107.6
8	0.023	0.9	150.7
10	0.032	0.9	160.4
20	0.044	2.9	211.1

Further observations of the wear tracks were made by the SEM. Figure 2 shows representative SEM images of the wear tracks for all investigated loads. For 2, 8, and 10 N of normal load (Figure 2a-c), the wear mechanism is mostly polishing and the damage to the coating is superficial. At 20 N (Figure 2d), traces of abrasive wear are evident, and it may be partially responsible for the increase of the coefficient of friction (Table 3).

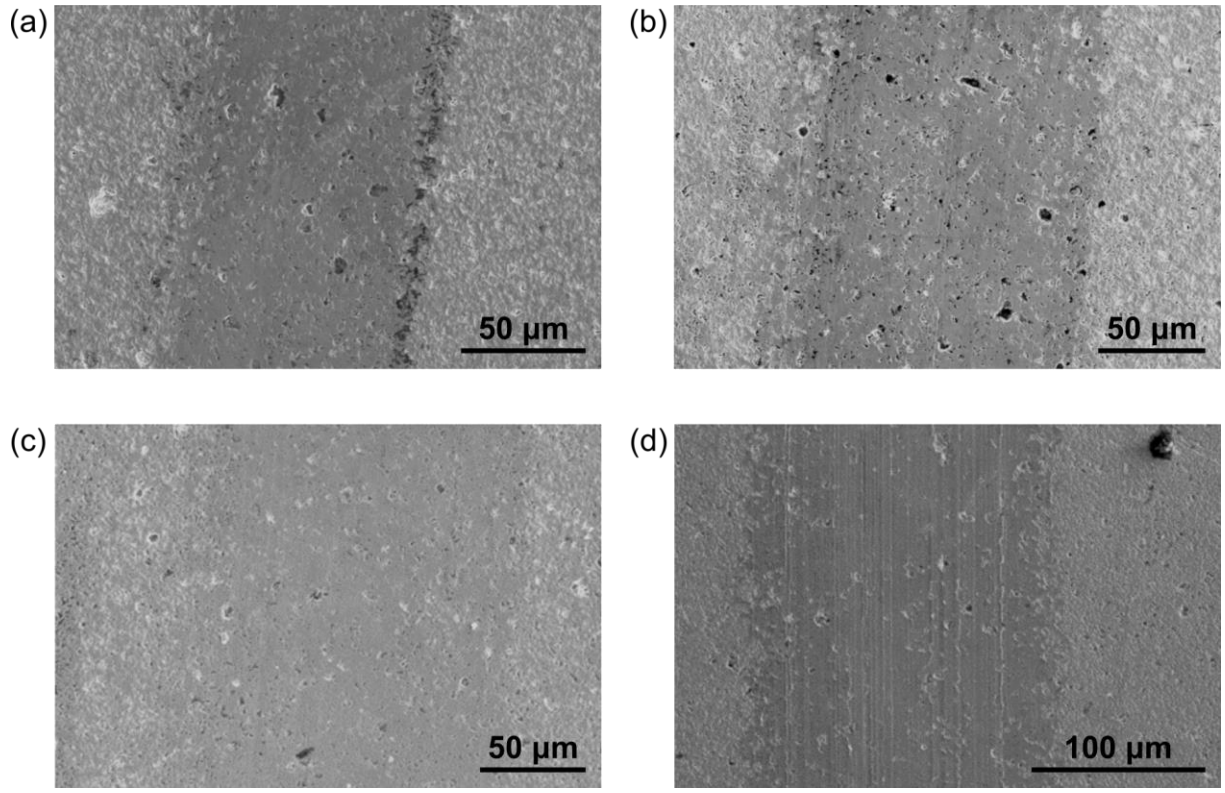

Figure 2. SEM images of the investigated wear tracks: a) 2 N, b) 8 N, c) 10 N and d) 20 N.

Overall, from either friction and wear measurements, or from SEM images, we cannot explain the behavior of the friction coefficient. Hence, it was necessary to go beyond macroscale and to use AFM and spectral Raman mapping to investigate further the basic tribological mechanisms. The approximate areas in the wear track used for different analytical techniques are marked on the profile map (Figure 3a). For comparison, the profile maps are provided for the other wear tracks as well (Figure 3b-d). The progressive transition from polishing to abrasive wear and increasing wear track depth and width are evident.

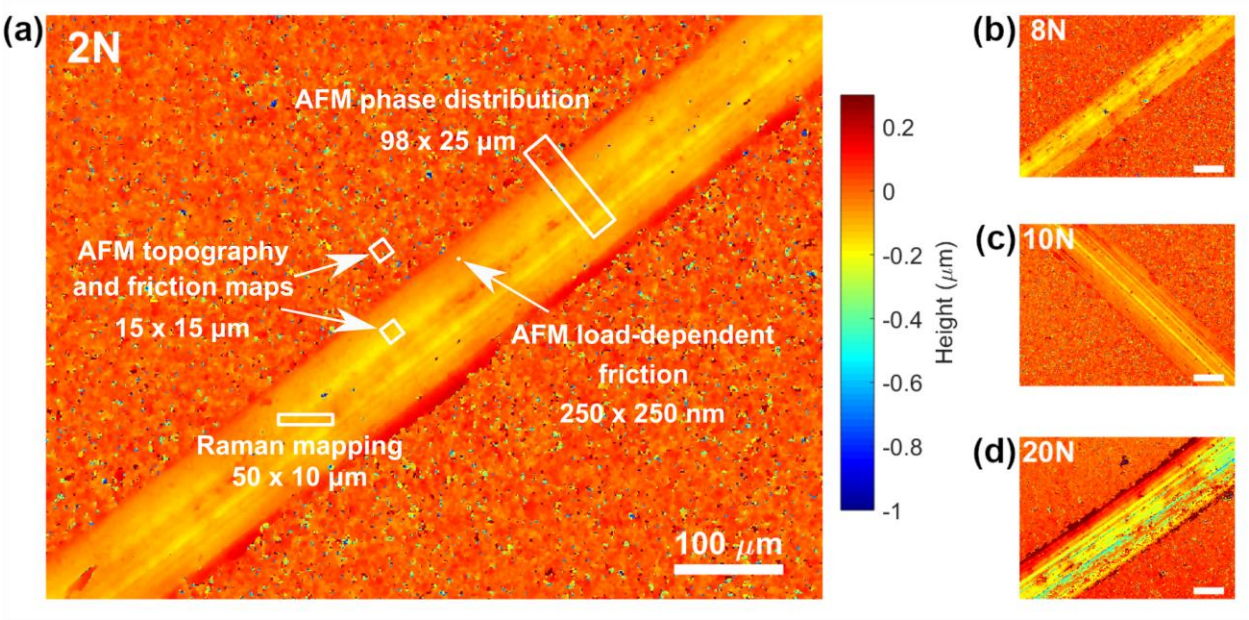

Figure 3. 3D optical profilometry of the investigated wear tracks. (a) The wear track obtained at 2 N with marked example areas analyzed in this paper. (b-d) 8 N, 10 N and 20 N wear tracks showing increasingly higher wear and progressive transition from polishing to abrasive wear. Scale bars correspond to 100 µm, height color bar applies to all.

3.3. Raman and spectral Raman mapping

Averaged Raman spectra over 561 points on each of the analyzed areas are shown in Figure 4; the curves were normalized by the average intensity of each measurement. At first, a large difference is observed in the tungsten oxide region (500-1000 cm^{-1}).[25,56] The wear tracks contain lower amounts of oxides than the as-deposited coating, meaning that most of the oxidation happened either during the deposition or, most likely, during the coating storage, and not during the tribo-tests. The oxide peaks on 2 N and 10 N samples are much weaker than the others, having the only prominent oxide peak at ~800 cm^{-1}, resembling WO_3.[56]

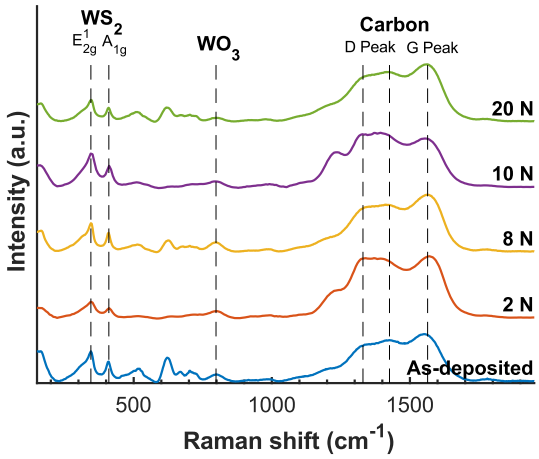

Figure 4. Averaged Raman spectra of the as-deposited coating and the investigated wear tracks.

As discussed by A. Ferrari and J. Robertson,[52] either the maximum peak height or the area under the peak can be used to determine the peak ratios. The two can be used interchangeably for disordered systems, while peak broadening in amorphous systems requires looking at the maximum peak height to include the information about less distorted aromatic rings. All peak ratios reported here were calculated from maximum peak heights. The average WS_2 peak intensity ratio, $I_{A_{1g}}/I_{E^1_{2g}}$, is between 0.61 and 0.68 for all spectra (Table 4), indicating no difference in crystallinity with increasing wear. The frequency difference between the peaks is between 65 and 67 cm^{-1}, which is within the set measurement resolution. This indicates that there is no significant difference in the WS_2 thickness and structure between different analyzed areas. From the frequency difference, we can assume the average layer thickness of WS_2 to be at least three layers (approx. 2 nm).[57] All samples show a very strong carbon signal. The I_D/I_G ratios were between 0.80 and 1.12, where the highest ratio can be observed in the 10 N sample and the lowest in the 8 N sample (**Table 4**), indicating the highest amount of graphitic structure on the 8 N wear track. Since those two samples experienced similar frictional behavior, we can conclude

that the observed difference in this range was either not significant, or that the chemical structure of carbon does not have an effect on the coefficient of friction.

Table 4. Peak ratios and frequency difference, as determined from the averaged Raman spectra.

Wear track	WS_2 peak ratio ($I_{A_{1g}}$ / $I_{E^1_{2g}}$)	Frequency difference ($f_{A_{1g}}$ - $f_{E^1_{2g}}$)	Carbon peak ratio (I_D / I_G)
As-deposited	0.68	65 cm^{-1}	0.81
2 N	0.61	67 cm^{-1}	0.97
8 N	0.68	65 cm^{-1}	0.80
10 N	0.64	67 cm^{-1}	1.12
20 N	0.65	65 cm^{-1}	0.86

The analysis revealed a significantly lower intensity of WS_2 peaks on the 2 N wear track, as compared to the ones obtained at higher loads; the highest I_{WS_2}/I_C peak ratio was observed in the 10 N wear track (Figure 5); in fact, the intensity at 10 N is comparable with the as-deposited coating. The low intensity of WS_2 at 2 N can be attributed to preferential wear of WS_2 and transfer of WS_2 to the sliding body at lower contact pressures. At low loads, the tribological properties are driven by constant removal of WS_2 from the surface, while carbon provides structural stability and prevents excessive wear. There is also lower energy input to the contact interface, which can slow the formation of the protective tribo-film. On the other hand, wear increases significantly above 10 N, as a result of much higher removal of material due to abrasion. Furthermore, the insufficient time for the formation of the tribo-film, or its instantaneous removal from the contact, results in accelerated wear of the coating. Consequently, we observe a slight decrease in WS_2 peak intensity at 20 N compared to 10 N.

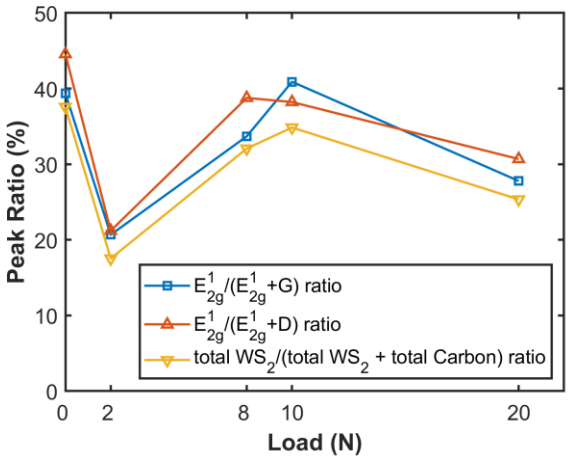

Figure 5. Peak ratios between WS_2 and carbon.

Threshold Raman maps, shown in Figure 6, represent the intensity of the WS_2 (A_{1g} mode, blue), carbon (G peak, red) and WO_3 (798 cm^{-1}, green) peaks in each measured point. Threshold maps were compiled from the intensity maps of each peak (Supporting Information, Figure S1). The threshold was set as 50% of the average intensity of the five highest peaks on the map, which assured that we could distinguish between the trace peak and actual peak intensity while not being influenced by a single high-intensity peak. The maps generally indicate the presence of all three compounds on all maps; however, their distribution differs. WS_2 appears very uniformly distributed, indicating no large differences in crystallinity. WO_3 is only present in spots across the samples, suggesting very local oxidation; more extensive coverage with WO_3 is observed on the as-deposited sample, further confirming that most of the oxidation happened during sample deposition or storage prior to the tribo-tests. The largest difference can be observed with carbon as the 2 N wear track contains much larger patches of carbon than the other samples. This further shows that WS_2 is either worn preferentially at lower loads or it is not formed in a sufficient amount, leaving behind larger patches of pure carbon.

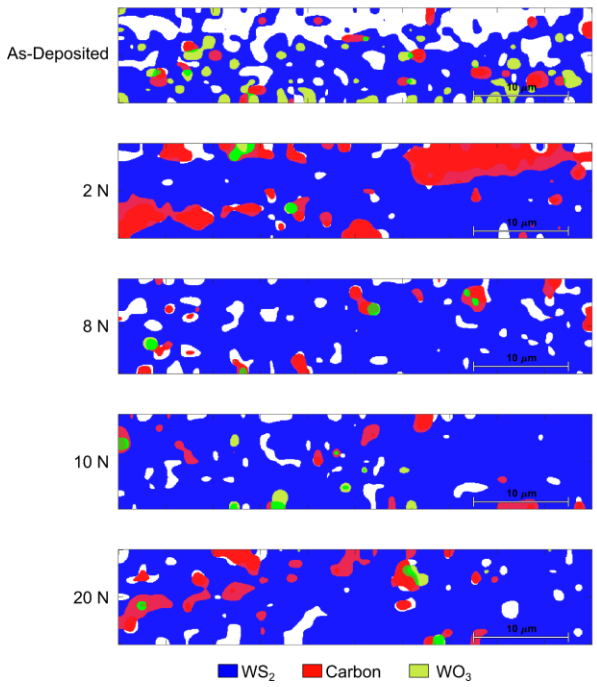

Figure 6. Threshold Raman maps, showing the peak intensities of WS_2 (blue), Carbon (red) and WO_3 (green).

3.4. Nanoscale characterization

The surface topography of the as-deposited W-S-C coating indicates compact columnar morphology (see Figure 7), with a significant amount of deep holes. The depth of the hole visible in Figure 7 is 1.75 μm and might indicate coating discontinuity (Supporting Information, Figure S2). However, the cross-section obtained by the SEM (see Figure 8d) reveals that the holes originate from the high substrate roughness, and the coating is uniformly aligned with the substrate topography. For the purpose of nano-tribological studies, we tried to avoid the holes and measure only on the flat surface of the coatings, except where this was not possible (e.g., large friction maps, where the analyzed area was much larger than the occurrence of holes on the surface).

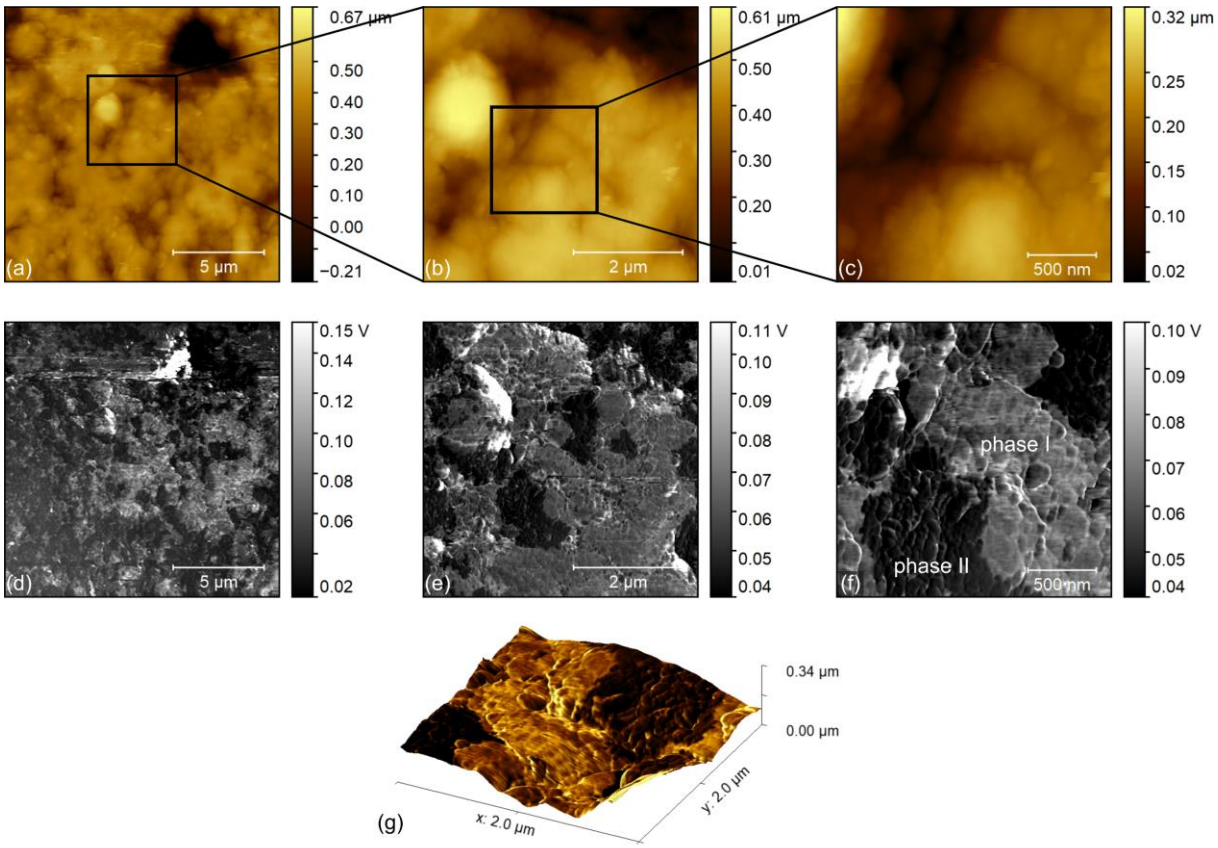

Figure 7. Structure of the as-deposited coating. Topography measured at: (a) 15 µm, (b) 5 µm and (c) 2 µm scan size. (d-f) The corresponding friction maps. (g) 3D topography overlayed by the friction signal at 2 µm scan size.

The topography and corresponding friction maps of the as-deposited coating in Figure 7 were obtained on the same spot at three different scan areas (15x15 µm, 5x5 µm, 2x2 µm), effectively zooming in on the surface to increase the resolution of the measured structures. The friction maps reveal the presence of two separate phases with contrasting frictional properties: high-friction phase (phase I) and low-friction phase (phase II). As evident from the overlay of frictional signal on topography (**Figure 7**g), these features do not follow the topography, meaning that the frictional contrast is not due to topographical effects and the two phases are uniformly embedded in the coating surface. The distribution of the phases in Figure 7 appears to

be uneven across the analyzed areas, as the periodicity of the features is larger than the scanning area (Supporting Information, Figure S3). On larger scans, each phase accounts for an almost equal amount (Supporting Information, Figure S3c). Observation of the surface structure at the smaller scale (Figure 7c and f) indicates that the low friction phase consists of 100-200 nm patches, which are clustered together to form a single phase. Similarly, the high friction phase of the sample also contains some smaller patches, but the general structure is less uniform.

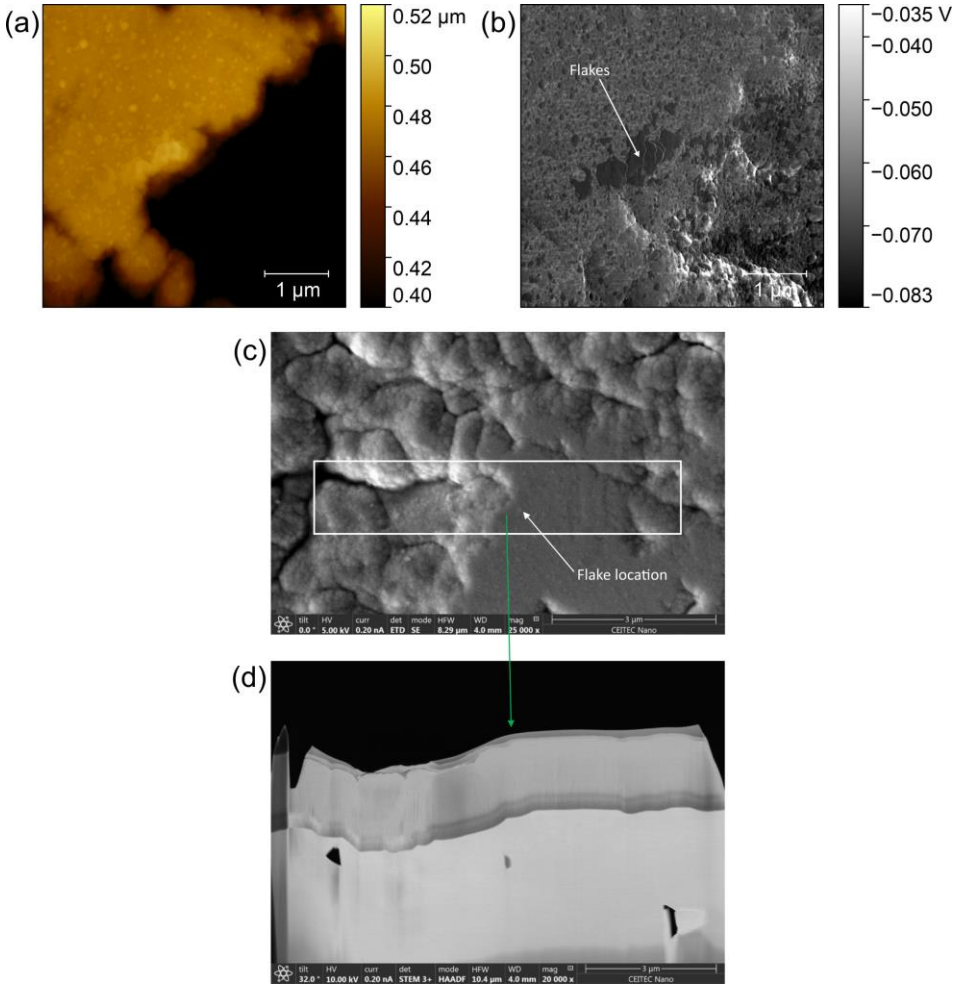

Figure 8. The same area on the edge of the wear track analyzed by AFM and SEM. (a) AFM topography of the coating – the scale is adjusted to increase the contrast of the flat area. (b) Friction map. (c) SEM topography displaying the location of the cut. The SEM image is rotated by 145°, compared to the AFM scans. (d) SEM cross-section.

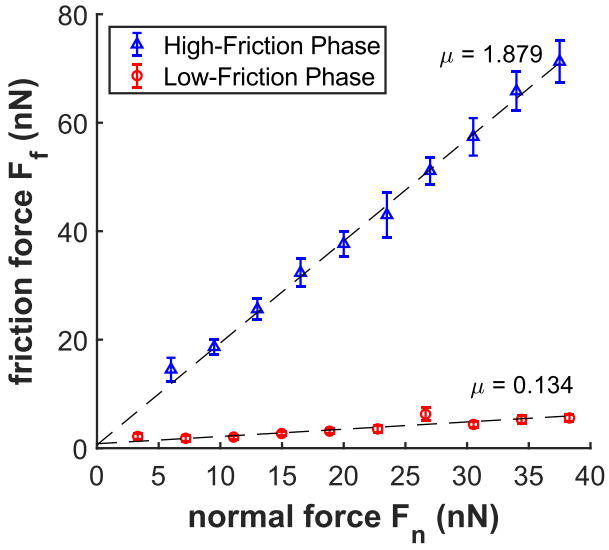

Figure 9. Nano-scale frictional behavior of the two phases: Low and high friction phases on the as-deposited W-S-C coating.

Figure 9 shows the frictional response on the high and low friction phases of the coating. The results reveal a substantial difference between the two analyzed regions, as the high friction phase exhibits approximately ten times higher friction than the low friction phase. Both phases exhibit similar linear behavior, indicating either quasi-flat (i.e., the contact area remains constant) or multi-asperity contact. This can be attributed to tip wear and flattening during the initial topography scans over large areas. As reported by L. Jingjing *et al.*[58] and D.S. Grierson *et al.*[59], the sharp apex of Si tip could fracture almost immediately after contact with the surface and further flatten during continuous scanning. No topographic changes were observed on the coating surfaces after the scanning.

Analyzing the surface topography (Figure 10, top and middle rows) of the measured wear tracks confirms the observation by SEM and optical profilometry (Figure 2 and Figure 3). At lower and intermediate loads, namely at 2 N and 8 N, we observe polishing wear, whereas at higher loads (20 N), the wear behavior transitions into abrasive. The surface morphology shows

that 2 N and 8 N wear tracks still contain the same amount of deep holes as the as-deposited coating, indicating generally low levels of wear. The roughness on the flat plateaus is comparable between 2 N and 8 N wear tracks (Supporting Information, Table S1). On the other hand, there are no signs of deep holes in the 20 N sample as the wear rates were much higher.

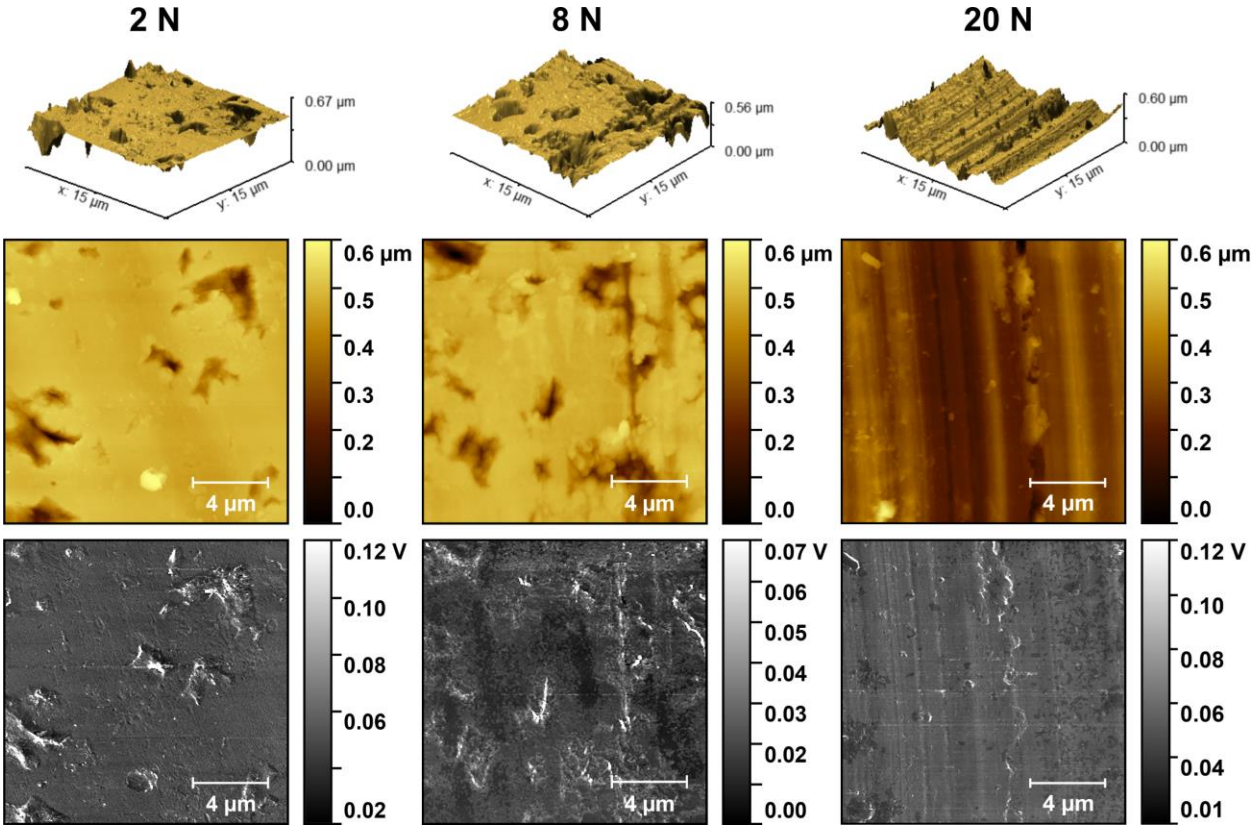

Figure 10. Surface structure (top: 3D representation, middle: surface topography, bottom: friction maps) of the wear track on the 2 N (left), 8 N (middle) and 20 N (right) samples. Flattening of the sample is clearly visible on 2 N and 8 N samples, whereas 20 N shows abrasive wear behavior.

Closer inspection of the wear track topography revealed the presence of multi-layered flat structures parallel to the sliding direction, such as the ones shown in Figure 11. The layered features, which are much flatter than the surrounding coating and exhibit low friction, were only found within the wear tracks. Therefore, they were produced by macroscopic sliding. Their shape

strongly resembles the WS_2 ordered tribolayer formed during tribo-reactions while sliding.[60] We identified structures with different shapes and sizes (ranging from 0.5 – 2.5 μm). However, the fully crystalline flakes within the wear tracks were very sparse. Furthermore, the shape of some of the multi-layered flakes, such as the central one seen on the 2 N wear track on Figure 11b, even resembles triangular geometry, which is a characteristic shape of a TMD crystal growth under a controlled environment.[61,62]

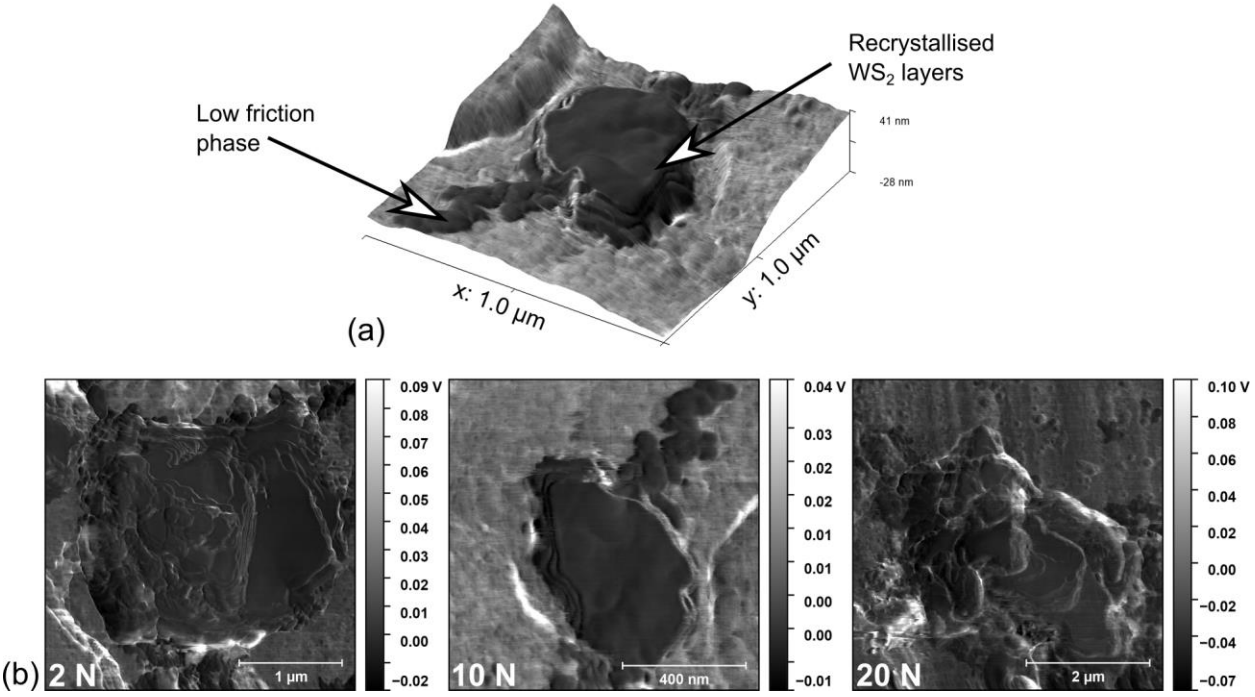

Figure 11. Tribo-film formation: (a) 3D view of a flake observed on the 10 N wear track, showing the difference in structure between low friction phase and layered tribo-film. The image is overlayed with raw friction signal. (b) Friction maps showing layered structures – flakes, found on the surface of different wear tracks, which indicate the formation of ordered TMD tribo-film in the sliding contact.

A similar feature can also be seen on Figure 8 – a wide multi-layered flake near the edge of the flat top surface. The same feature, however, could not be observed either by the SEM or by

TEM. We performed TEM on the cross-section (Figure 12a) cut by FIB from such a flat area, but could not detect the observed feature from the AFM. Some randomly oriented ordered structures can be seen on the surface and below the surface, but they are on a much smaller scale, measuring only a few nanometers. However, it is worth mentioning that the flat areas are very small, and it is likely we were not able to extract the sample exactly from the spot. In fact, clear traces of ordered structure oriented parallel to the surface can be seen on another part of the wear track (Figure 12b), which was not analyzed by AFM.

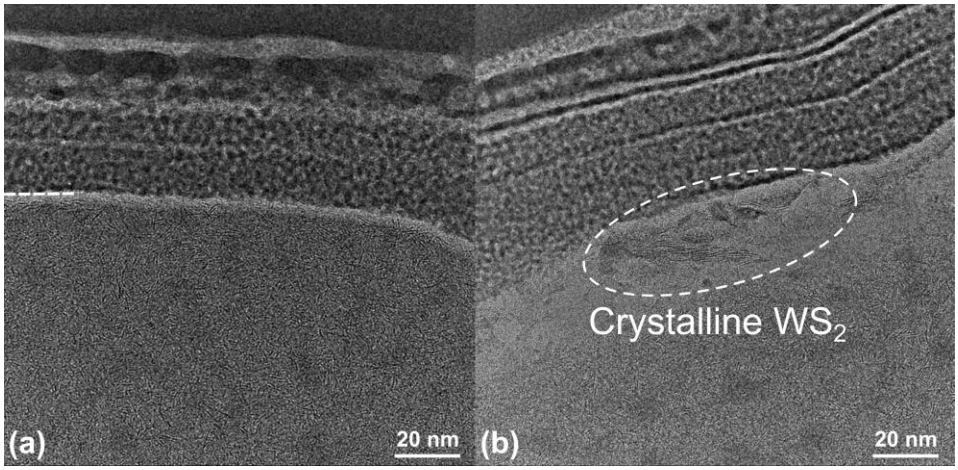

Figure 12. Cross-sectional TEM images of the wear track: (a) the region from **Figure 8**, (b) the other edge of the same wear track. The coating surface is shown by the dashed white line (center left).

The frictional behavior inside the wear track is shown in Figure 13. The values of frictional force of the low friction phase are comparable to the ones of the bare coating, with no observable difference in behavior or magnitude. On the other hand, the absolute friction values and behavior on the high friction phase reduce significantly, which can be attributed to the flattening of the surface due to polishing wear. For example, the nano-scale surface roughness of the high friction phase, obtained over 225x225 nm area, decreased from 2.31 nm on the bulk coating to only 0.54

nm within the wear track (Supporting Information, Table S2). Furthermore, sliding at reasonably low loads (that would result in polishing wear) may also contribute to the passivation of some dangling bonds on the surface, thus further reducing nano-scale frictional response.

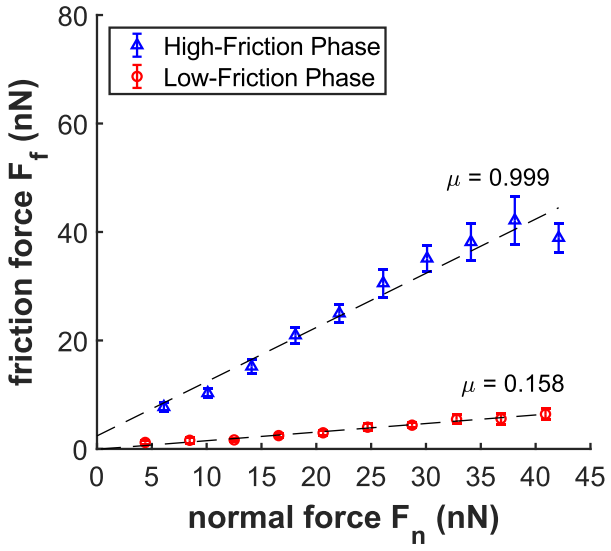

Figure 13. Load-dependent friction on the two phases inside the wear track. High friction phase measured within 2 N wear track and low friction phase within 8 N wear track.

Figure 14 displays the amount of low friction phase across the width of the wear track. The measurements were performed perpendicular to the sliding direction and the coordinate system was placed on the edge of the wear track for all three of the analyzed samples. Figure 14a and Figure 14b show the topography and the frictional map of the 8 N wear track, on which the ratios were obtained. The dashed line represents the location of the edge of the wear track. The low-friction phase corresponds to dark-blue points and high-friction to a lighter blue. Regions with higher values of friction (green, yellow, red) are a consequence of surface topography or surface contamination. These regions directly correspond to the holes on the topography scan. In contrast, the boundaries between the two phases are not visible in the topography image. The

presented ratio was determined as the amount of low friction phase against the total corresponding area.

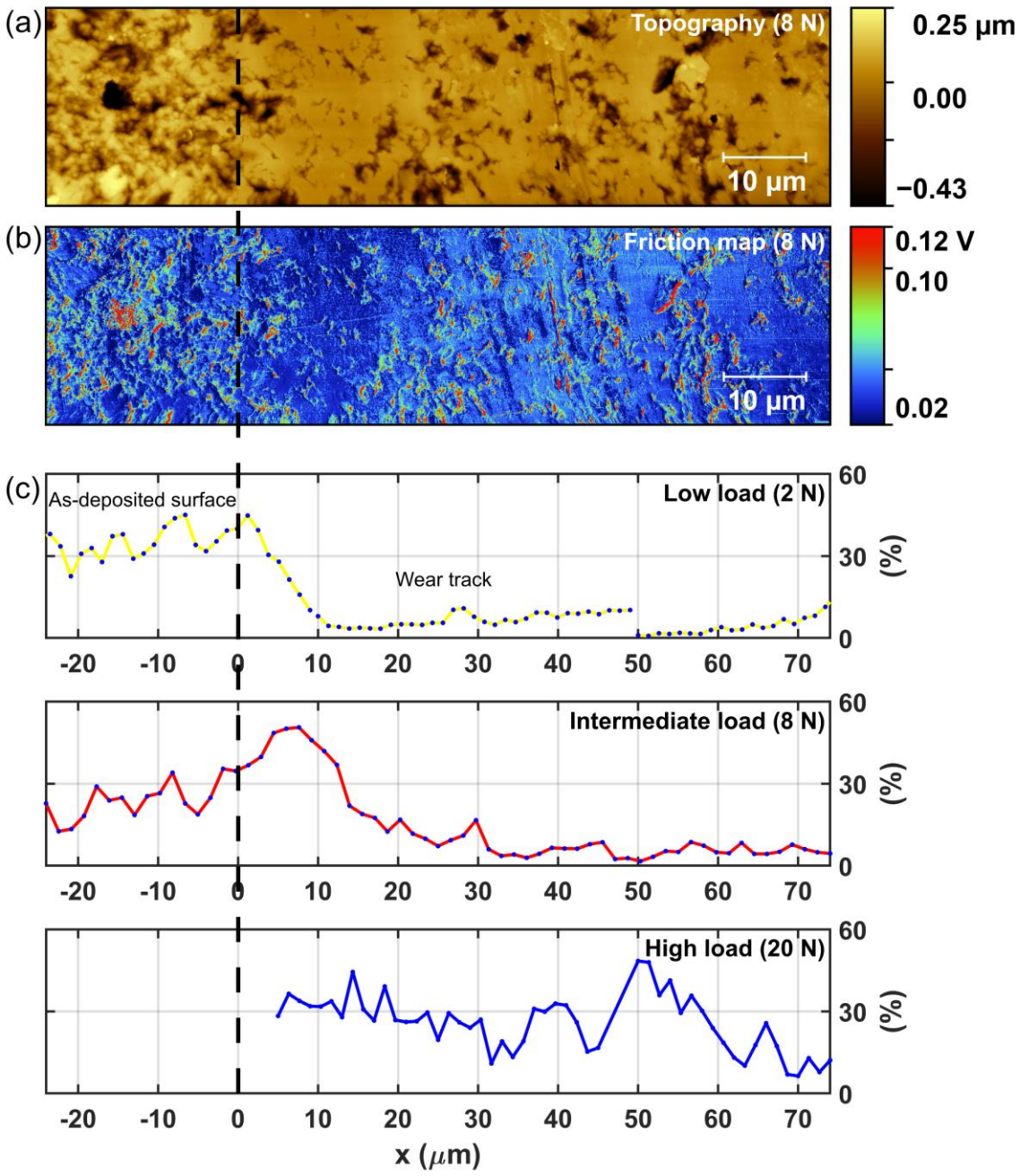

Figure 14. The amount of low friction phase across the wear track. (a) 98x15 um topography scan of the 8 N wear track. (b) The corresponding friction map. (c) The ratios for 2 N, 8 N and 20 N wear tracks.

Comparing the distributions on the wear tracks obtained at low (2 N), intermediate (8 N) and high (20 N) normal loads reveals significantly different characteristics. As expected, there is no observable difference in the regions outside of the wear tracks, with the low friction phase remaining between 20-40% in all the measured points. The other edge of the wear track was not reached on any of the samples, due to wear tracks being wider than the AFM scan size limit of 100 μm (see Figure 3).

At low loads (2 N), the amount of the low friction phase drops immediately at the edge of the wear track and remains low until the end. There are some slight local increases in a few points, but the amount always stays below 10%. At intermediate loads (8 N), we can observe an increased amount of low friction phase up to 50% within the first 15 μm of the wear track, indicating transfer and accumulation of the low friction phase towards the sides. The concentration then decreases to 15-20% until 30 μm and finally drops to below 10%, reaching similar distribution than at low loads.

On the other hand, significantly different behavior can be observed in the last wear track obtained at 20 N. The amount of the low friction phase is much higher than in the other two, and it even increases to almost 50% towards the center of the wear track. This suggests that at higher contact loads, both phases wear at similar rates.

4 DISCUSSION

Firstly, we must note that some of the friction measurements with different probes of the same type followed the 2/3 power law (Supporting Information, Figure S4), thus indicating adhesive behavior according to *Hertz-plus offset* model,[63] similar to previously reported results by J. Zekonyte *et al.*[44,45] on W-S-C and W-S-C-Cr coatings. However, the probe shape can strongly

influence the resulting contact properties.[64] To accurately analyze the samples accurately and minimize the potential error arising from the probe shape, all the quantitative friction measurements reported in this paper were performed using the same probe, which had undergone pre-wearing during the initial topography tests. This assured minimum wear during the frictional experiments and, therefore, consistent probe shape throughout the friction measurements.

The observed columnar topography (Figure 7) of the as-deposited W-S-C coatings is comparable to the previously reported structures of similar coatings.[14,65] The coating thickness is uniform, but the overall surface roughness is high when compared to the thickness. As shown in the cross-section (Figure 8), the surface roughness is a consequence of the substrate roughness, rather than coating non-uniformity. Nonetheless, surface roughness did not affect the tribological performance.

The as-deposited coating surface consists of two separate phases, with significantly different nano-scale frictional properties: (i) high friction phase, with a coefficient of friction above 1, indicating the onset of chemical bonding between the tip and the surface, and (ii) low friction phase, with a coefficient of friction approximately 0.15, exhibiting easy sliding. The size and the shape of the observed phases appear random, while their distribution on the as-deposited surface reveals that the two phases attribute to approximately equal amounts across the entire coating. Our results show that the phases are completely separated, with clearly defined borders in between. The feature sizes (e.g., the size of a single continuous low-friction section) can range anywhere from 100 nm to over 10 μm. According to E. Serpini *et al.*,[46] nano-scale friction of pure sputtered amorphous TMD films is reported to be significantly higher than that of the crystalline material. Similarly, amorphous carbon also exhibits high nano-scale friction,[66] especially under ambient conditions.[63] From our observations, we can conclude that the high

friction phase corresponds to a highly disordered solution of WS_2 and carbon, while low friction represents locally nano-crystalline WS_2. The highly disordered structure could contain high amounts of dangling bonds, thus resulting in chemical bonding with the tip during sliding and consequently increased nano-scale friction.

Frictional response within the wear tracks shows some degree of friction reduction of the high friction phase, compared to the respective measurement on the as-deposited bulk coating. This reduction may be linked to flattening of the surface due to polishing wear and passivation of dangling bonds during sliding. We can again identify the two separated phases; however, their distribution is changed and shows load dependence. Whereas the as-deposited coating shows a reasonably even distribution of the phases over the entire coating surface, the distribution across the wear track profiles vary at different loads. This indicates the uneven wear of the two phases. At low loads, the low friction phase wears preferentially, leaving a much higher concentration of the high friction phase on the wear track. A similar case is observed at 8 N, but the amount of the low friction phase is slightly higher, particularly closer to the edge of the wear track. On the other hand, at 20 N, the high and abrasive wear results in continuous removal of the material. Therefore, the ratio of high and low friction phases is similar to that of the as-deposited surface.

Furthermore, we have observed traces of fully recrystallized WS_2 tribo-film being formed in the wear tracks in the form of multi-layered flakes. The coverage of the wear tracks with such crystalline features is low, and they occur randomly across the analyzed areas. This is somewhat contradictory to the previously believed sliding mechanisms of TMD and TMD-C coatings[14,67] and indicates that the tribo-film formation is very local within the wear tracks. It is likely that the structural transformation (from amorphous W-S-C coating into crystalline WS_2 tribolayer) occurs only at the asperities in the contact where the energy input is the highest; in fact, the real

contact area represents only a fraction of the total area. The tribo-film is only formed when enough energy is introduced in the contact, rather than being formed continuously. Therefore, even low coverage by WS_2 tribolayer can still provide a significant reduction of friction. It is worth noting that low amounts and sparse distribution of such crystalline layers may also present a challenge in the observation of tribo-film formation by TEM; for coatings with low amounts of tribo-film in the wear track, these areas can easily be missed. As seen from the example in this paper, the thickness of the formed flakes was only a few layers, and they could easily be removed or damaged during sample preparation or further handling. Furthermore, the inability to see the exact location of the flake by SEM requires relying on the reference AFM scans to identify the suitable area for analysis.

The observed nano-scale frictional properties, namely the coefficient of friction, differ quite substantially from the measurements on the macro-scale; nevertheless, they can be understood by the same principles. Since the AFM tip represents a single asperity[39] and the ratios between the phases on the as-deposited coating surface are close to 1:1, it follows that, on average, only half of the asperities in contact would initially interact with the potentially chemically reactive high-friction phase. Interaction between the reactive surface and the sliding body then results in immediate passivation of the surface dangling bonds and, therefore, a significant reduction of the friction force.

Furthermore, some material transfer to the sliding body can occur, thus further modifying the interface structure. The sliding interface is therefore established within the coating, rather than between the sliding body and the coating, meaning that the frictional properties are mainly driven by the shear strength of the coating. Furthermore, the tribo-film, which is formed when

the introduced energy to the contact could damage the coating, can further protect the surface further and reduce friction.

Finally, we have shown that using AFM to identify the presence of crystalline tribo-film and study its structure is a very powerful alternative to standard wear track analysis. It does not require specific sample preparation and has a much lower energy input during the measurement, thus preventing the sample from potential alterations, which can occur with other beam-based characterization techniques.

5. CONCLUSIONS

AFM analysis of W-S-C coatings revealed a two-phase structure of the coatings. The phases exhibit notably different frictional characteristics, with an order of magnitude difference in absolute values of lateral forces between them. Raman analysis has revealed obvious contrast between the regions either rich in carbon or rich in WS_2 and with various crystallinity across the analyzed area, leading to a conclusion that the two phases correspond to an amorphous solution of WS_2 and C (high-friction) and nano-crystalline WS_2 (low-friction) regions.

Frictional mapping within the wear tracks has unveiled different distributions of low and high friction phases across the wear tracks, according to the applied loads during the macro-scale tribo-tests. At low loads, only the high friction phase remained, indicating preferential wear of low friction phase. At intermediate loads, the low friction phase was abundant near the edges but almost depleted towards the center of the wear track. At high loads, we observed a completely different distribution; the amount of low friction phase was higher than at lower loads but remained constant across the measured area. It can be correlated to considerably higher wear rates that were observed at 20 N. We can conclude that the high friction phase provides good

wear resistance and structural stability, while the low friction phase provides good sliding properties.

Large, flat, and multi-layered WS_2 flakes were identified within the wear tracks by AFM analysis. The high resolution of AFM allows a very detailed examination of the surface and can reveal the features which would be impossible to identify with other techniques. Up to now, the crystallinity of the TMD tribo-film has mostly been examined by TEM observation. However, our analysis shows very low coverage of the wear track with the fully crystalline tribo-film. Performing TEM analysis on rough coatings such as those presented in this study would be challenging without precisely knowing the location of the crystalline tribo-film. Additionally, the low coverage of the wear tracks with the flakes indicates very local recrystallization of WS_2 where the contact conditions (pressure, temperature) exceed the threshold of energy input required for structural transformation.

ASSOCIATED CONTENT

Supporting Information. The following files are available free of charge.

Raman surface maps, additional topography of the as-deposited coating, surface roughness alternative load-dependent measurements. (PDF)

AUTHOR INFORMATION

Corresponding Authors

* Ales Rapuc: – a.rapuc@soton.ac.uk

* Tomas Polcar: – t.polcar@soton.ac.uk

Author Contributions

The manuscript was written through contributions of all authors. All authors have given approval to the final version of the manuscript.

Notes

The authors declare no competing financial interest.

ACKNOWLEDGMENT

Ales Rapuc, Teodor Huminiuc, Albano Cavaleiro and Tomas Polcar were funded by H2020 MSCA ITN project Solution No. 721642. Kosta Simonovic and Tomas Polcar received funding from the project OPVVV Novel nanostructures for engineering applications No. CZ.02.1.01/0.0/0.0/16_026/0008396. Teodor Huminiuc received support from CEITEC Nano Research Infrastructure (ID LM2015041, MEYS CR, 2016–2019).

REFERENCES

(1) REGULATION (EU) 2019/631 OF THE EUROPEAN PARLIAMENT AND OF THE COUNCIL of 17 April 2019 Setting CO2 Emission Performance Standards for New Passenger Cars and for New Light Commercial Vehicles, and Repealing Regulations (EC) No 443/2009 and (EU) No 510/201. *Off. J. Eur. Union* **2019**, No. L 111, 13–53.

(2) Holmberg, K.; Erdemir, A. Influence of Tribology on Global Energy Consumption, Costs and Emissions. *Friction*. 2017, pp 263–284. https://doi.org/10.1007/s40544-017-0183-5.

(3) Carpick, R. W.; Jackson, A.; Sawyer, W. G.; Argibay, N.; Lee, P.; Pachon, A.; Gresham, R. M. The Tribology Opportunities Study: Can Tribology Save a Quad? *Tribol. Lubr. Technol.* **2016**, *72* (5), 44–45.

(4) Roberts, E. W. Thin Solid Lubricant Films in Space. *Tribol. Int.* **1990**, *23* (2), 95–104. https://doi.org/10.1016/0301-679X(90)90042-N.

(5) Fan, X.; Wang, L. Highly Conductive Ionic Liquids toward High-Performance Space-Lubricating Greases. *ACS Appl. Mater. Interfaces* **2014**, *6* (16), 14660–14671. https://doi.org/10.1021/am503941e.

(6) Reeves, C. J.; Menezes, P. L.; Lovell, M. R.; Jen, T.-C. Tribology of Solid Lubricants. In *Tribology for Scientists and Engineers*; Springer New York: New York, NY, 2013; Vol. 9781461419, pp 447–494. https://doi.org/10.1007/978-1-4614-1945-7_13.

(7) Scharf, T. W.; Prasad, S. V. Solid Lubricants: A Review. *J. Mater. Sci.* **2013**, *48* (2), 511–531. https://doi.org/10.1007/s10853-012-7038-2.

(8) Minami, I. Ionic Liquids in Tribology. *Molecules* **2009**, *14* (6), 2286–2305. https://doi.org/10.3390/molecules14062286.

(9) Zhou, F.; Liang, Y.; Liu, W. Ionic Liquid Lubricants: Designed Chemistry for Engineering Applications. *Chem. Soc. Rev.* **2009**, *38* (9), 2590. https://doi.org/10.1039/b817899m.

(10) Palacio, M.; Bhushan, B. A Review of Ionic Liquids for Green Molecular Lubrication in Nanotechnology. *Tribol. Lett.* **2010**, *40* (2), 247–268. https://doi.org/10.1007/s11249-010-9671-8.

(11) Kawada, S.; Watanabe, S.; Kondo, Y.; Tsuboi, R.; Sasaki, S. Tribochemical Reactions of Ionic Liquids under Vacuum Conditions. *Tribol. Lett.* **2014**, *54* (3), 309–315. https://doi.org/10.1007/s11249-014-0342-z.

(12) Voevodin, A. A.; O'Neill, J. P.; Zabinski, J. S. Nanocomposite Tribological Coatings for Aerospace Applications. *Surf. Coatings Technol.* **1999**, *116–119*, 36–45. https://doi.org/10.1016/S0257-8972(99)00228-5.

(13) Polcar, T.; Evaristo, M.; Cavaleiro, A. Comparative Study of the Tribological Behavior of Self-Lubricating W-S-C and Mo-Se-C Sputtered Coatings. *Wear* **2009**, *266* (3–4), 388–392. https://doi.org/10.1016/j.wear.2008.04.011.

(14) Polcar, T.; Cavaleiro, A. Review on Self-Lubricant Transition Metal Dichalcogenide Nanocomposite Coatings Alloyed with Carbon. *Surf. Coatings Technol.* **2011**, *206* (4), 686–695. https://doi.org/10.1016/j.surfcoat.2011.03.004.

(15) Lu, J.; Yang, S.; Wang, J.; Xue, Q. Mechanical and Tribological Properties of Ni-Based Alloy/CeF3/Graphite High Temperature Self-Lubricating Composites. *Wear* **2001**, *249* (12), 1070–1076. https://doi.org/10.1016/S0043-1648(01)00846-8.

(16) Raadnui, S.; Mahathanabodee, S.; Tongsri, R. Tribological Behaviour of Sintered 316L Stainless Steel Impregnated with MoS2 Plain Bearing. *Wear* **2008**, *265* (3–4), 546–553. https://doi.org/10.1016/j.wear.2007.11.014.

(17) Polcar, T.; Cavaleiro, A. Self-Adaptive Low Friction Coatings Based on Transition Metal Dichalcogenides. *Thin Solid Films* **2011**, *519* (12), 4037–4044. https://doi.org/10.1016/j.tsf.2011.01.180.

(18) Martin, J. M.; Donnet, C.; Le Mogne, T.; Epicier, T. Superlubricity of Molybdenum Disulphide. *Phys. Rev. B* **1993**, *48* (14), 10583–10586. https://doi.org/10.1103/PhysRevB.48.10583.

(19) Yaqub, T. Bin; Vuchkov, T.; Evaristo, M.; Cavaleiro, A. DCMS Mo-Se-C Solid Lubricant Coatings – Synthesis, Structural, Mechanical and Tribological Property Investigation. *Surf. Coatings Technol.* **2019**, *378* (September), 124992. https://doi.org/10.1016/j.surfcoat.2019.124992.

(20) A.R. Lansdown. *Molybdenum Disulphide Lubrication*, 1st ed.; Elsevier, 1999.

(21) Spalvins, T.; Przybyszewski, J. S. Deposition of Sputtered Molybdenum Disulphide Films and Friction Characteristics of Such Films in Vacuum. *Vacuum* **1968**, *18* (8), 496. https://doi.org/10.1016/0042-207X(68)90504-6.

(22) Przybyszewski, J. S.; Spalvins, T. Friction and Contact Resistance during Sliding in Vacuum of Some Low-Resistivity Metals Lubricated with Sputtered Molybdenum Disulfide Films. *Note, Nasa Tech.* **1969**.

(23) Spalvins, T. Friction Characteristics of Sputtered Solid Film Lubricants. *NASA Tech. Memo. TM X- 52819* **1970**.

(24) Teer, D. G.; Hampshire, J.; Fox, V.; Bellido-Gonzalez, V. The Tribological Properties of MoS2/Metal Composite Coatings Deposited by Closed Field Magnetron Sputtering. *Surf. Coatings Technol.* **1997**, *94–95*, 572–577. https://doi.org/10.1016/S0257-8972(97)00498-2.

(25) Polcar, T.; Gustavsson, F.; Thersleff, T.; Jacobson, S.; Cavaleiro, A. Complex Frictional

Analysis of Self-Lubricant W-S-C/Cr Coating. *Faraday Discuss.* **2012**, *156*, 383. https://doi.org/10.1039/c2fd00003b.

(26) Stupp, B. C. Synergistic Effects of Metals Co-Sputtered with MoS2. *Thin Solid Films* **1981**, *84* (3), 257–266. https://doi.org/10.1016/0040-6090(81)90023-7.

(27) Holbery, J. D.; Pflueger, E.; Savan, A.; Gerbig, Y.; Luo, Q.; Lewis, D. B.; Munz, W.-D. Alloying MoS2 with Al and Au: Structure and Tribological Performance. *Surf. Coatings Technol.* **2003**, *169–170*, 716–720. https://doi.org/10.1016/S0257-8972(03)00203-2.

(28) Xu, S.; Gao, X.; Hu, M.; Sun, J.; Wang, D.; Zhou, F.; Weng, L.; Liu, W. Morphology Evolution of Ag Alloyed WS2 Films and the Significantly Enhanced Mechanical and Tribological Properties. *Surf. Coatings Technol.* **2014**, *238*, 197–206. https://doi.org/10.1016/j.surfcoat.2013.10.074.

(29) Wahl, K. J.; Seitzman, L. E.; Bolster, R. N.; Singer, I. L. Low-Friction, High-Endurance, Ion-Beam-Deposited PbMoS Coatings. *Surf. Coatings Technol.* **1995**, *73* (3), 152–159. https://doi.org/10.1016/0257-8972(94)02383-2.

(30) Voevodin, A. A.; Zabinski, J. S. Supertough Wear-Resistant Coatings with “chameleon” Surface Adaptation. *Thin Solid Films* **2000**, *370* (1), 223–231. https://doi.org/10.1016/S0040-6090(00)00917-2.

(31) Nossa, A.; Cavaleiro, A. Mechanical Behaviour of W-S-N and W-S-C Sputtered Coatings Deposited with a Ti Interlayer. *Surf. Coatings Technol.* **2003**, *163–164*, 552–560. https://doi.org/10.1016/S0257-8972(02)00622-9.

(32) Gu, L.; Ke, P.; Zou, Y.; Li, X.; Wang, A. Amorphous Self-Lubricant MoS2-C Sputtered

Coating with High Hardness. *Appl. Surf. Sci.* **2015**, *331*, 66–71. https://doi.org/10.1016/j.apsusc.2015.01.057.

(33) Evaristo, M.; Polcar, T.; Cavaleiro, A. Can W-Se-C Coatings Be Competitive to W-S-C Ones? *Plasma Process. Polym.* **2009**, *6* (SUPPL. 1), 92–95. https://doi.org/10.1002/ppap.200930414.

(34) Nossa, A.; Cavaleiro, A. The Influence of the Addition of C and N on the Wear Behaviour of W–S–C/N Coatings. *Surf. Coatings Technol.* **2001**, *142–144*, 984–991. https://doi.org/10.1016/S0257-8972(01)01249-X.

(35) Isaeva, L.; Sundberg, J.; Mukherjee, S.; Pelliccione, C. J.; Lindblad, A.; Segre, C. U.; Jansson, U.; Sarma, D. D.; Eriksson, O.; Kádas, K. Amorphous W-S-N Thin Films: The Atomic Structure behind Ultra-Low Friction. *Acta Mater.* **2015**, *82*, 84–93. https://doi.org/10.1016/j.actamat.2014.08.043.

(36) Gustavsson, F.; Jacobson, S.; Cavaleiro, A.; Polcar, T. Ultra-Low Friction W-S-N Solid Lubricant Coating. *Surf. Coatings Technol.* **2013**, *232*, 541–548. https://doi.org/10.1016/j.surfcoat.2013.06.026.

(37) Randall, N. X. Experimental Methods in Tribology. In *Tribology for Scientists and Engineers: From Basics to Advanced Concepts*; Springer New York, 2013; Vol. 9781461419457, pp 141–175. https://doi.org/10.1007/978-1-4614-1945-7_4.

(38) Bhushan, B. Nanotribology and Nanomechanics. *Wear* **2005**, *259* (7–12), 1507–1531. https://doi.org/10.1016/j.wear.2005.01.010.

(39) Szlufarska, I.; Chandross, M.; Carpick, R. W. Recent Advances in Single-Asperity

Nanotribology. *J. Phys. D. Appl. Phys.* **2008**, *41* (12), 123001. https://doi.org/10.1088/0022-3727/41/12/123001.

(40) Dienwiebel, M.; Verhoeven, G. S.; Pradeep, N.; Frenken, J. W. M.; Heimberg, J. A.; Zandbergen, H. W. Superlubricity of Graphite. *Phys. Rev. Lett.* **2004**, *92* (12), 1–4. https://doi.org/10.1103/PhysRevLett.92.126101.

(41) Lin, L. Y.; Kim, D. E.; Kim, W. K.; Jun, S. C. Friction and Wear Characteristics of Multi-Layer Graphene Films Investigated by Atomic Force Microscopy. *Surf. Coatings Technol.* **2011**, *205* (20), 4864–4869. https://doi.org/10.1016/j.surfcoat.2011.04.092.

(42) Lee, C.; Li, Q.; Kalb, W.; Liu, X. Z.; Berger, H.; Carpick, R. W.; Hone, J. Frictional Characteristics of Atomically Thin Sheets. *Science (80-.).* **2010**, *328* (5974), 76–80. https://doi.org/10.1126/science.1184167.

(43) Fang, L.; Liu, D.-M.; Guo, Y.; Liao, Z.-M.; Luo, J.-B.; Wen, S.-Z. Thickness Dependent Friction on Few-Layer MoS2, WS2, and WSe2. *Nanotechnology* **2017**, *28* (24). https://doi.org/10.1088/1361-6528/aa712b.

(44) Zekonyte, J.; Polcar, T. Friction Force Microscopy Analysis of Self-Adaptive W-S-C Coatings: Nanoscale Friction and Wear. *ACS Appl. Mater. Interfaces* **2015**, *7* (38), 21056–21064. https://doi.org/10.1021/acsami.5b05546.

(45) Zekonyte, J.; Cavaleiro, A.; Polcar, T. Frictional Properties of Self-Adaptive Chromium Doped Tungsten-Sulfur- Carbon Coatings at Nanoscale. *Appl. Surf. Sci.* **2014**, *303*, 381–387. https://doi.org/10.1016/j.apsusc.2014.03.010.

(46) Serpini, E.; Rota, A.; Valeri, S.; Ukraintsev, E.; Rezek, B.; Polcar, T.; Nicolini, P.

Nanoscale Frictional Properties of Ordered and Disordered MoS2. *Tribol. Int.* **2019**, *136* (March), 67–74. https://doi.org/10.1016/j.triboint.2019.03.004.

(47) Goldstein, J. I.; Newbury, D. E.; Echlin, P.; Joy, D. C.; Lyman, C. E.; Lifshin, E.; Sawyer, L.; Michael, J. R. *Scanning Electron Microscopy and X-Ray Microanalysis*; Springer US: Boston, MA, 2003. https://doi.org/10.1007/978-1-4615-0215-9.

(48) Vilá, R. A.; Rao, R.; Muratore, C.; Bianco, E.; Robinson, J. A.; Maruyama, B.; Glavin, N. R. In Situ Crystallization Kinetics of Two-Dimensional MoS 2. *2D Mater.* **2017**, *5* (1), 011009. https://doi.org/10.1088/2053-1583/aa9674.

(49) Hutter, J. L.; Bechhoefer, J. Calibration of Atomic-Force Microscope Tips. *Rev. Sci. Instrum.* **1993**, *64* (7), 1868–1873. https://doi.org/10.1063/1.1143970.

(50) Ogletree, D. F.; Carpick, R. W.; Salmeron, M. Calibration of Frictional Forces in Atomic Force Microscopy. *Rev. Sci. Instrum.* **1996**, *67* (9), 3298–3306. https://doi.org/10.1063/1.1147411.

(51) Casiraghi, C.; Ferrari, A. C.; Robertson, J. Raman Spectroscopy of Hydrogenated Amorphous Carbons. *Phys. Rev. B* **2005**, *72* (8), 085401. https://doi.org/10.1103/PhysRevB.72.085401.

(52) Ferrari, A. C.; Robertson, J. Interpretation of Raman Spectra of Disordered and Amorphous Carbon. *Phys. Rev. B* **2000**, *61* (20), 14095–14107. https://doi.org/10.1103/PhysRevB.61.14095.

(53) Zhao, W.; Ghorannevis, Z.; Amara, K. K.; Pang, J. R.; Toh, M.; Zhang, X.; Kloc, C.; Tan, P. H.; Eda, G. Lattice Dynamics in Mono- and Few-Layer Sheets of WS2 and WSe2.

Nanoscale **2013**, *5* (20), 9677–9683. https://doi.org/10.1039/c3nr03052k.

(54) Molina-Sánchez, A.; Wirtz, L. Phonons in Single-Layer and Few-Layer MoS2 and WS2. *Phys. Rev. B - Condens. Matter Mater. Phys.* **2011**, *84* (15), 1–8. https://doi.org/10.1103/PhysRevB.84.155413.

(55) Wang, F.; Kinloch, I. A.; Wolverson, D.; Tenne, R.; Zak, A.; O'Connell, E.; Bangert, U.; Young, R. J. Strain-Induced Phonon Shifts in Tungsten Disulfide Nanoplatelets and Nanotubes. *2D Mater.* **2017**, *4* (1). https://doi.org/10.1088/2053-1583/4/1/015007.

(56) Xu, S.; Liu, Y.; Gao, M.; Kang, K.-H.; Shin, D.-G.; Kim, D.-E. Superior Lubrication of Dense/Porous-Coupled Nanoscale C/WS2 Multilayer Coating on Ductile Substrate. *Appl. Surf. Sci.* **2019**, *476* (October 2018), 724–732. https://doi.org/10.1016/j.apsusc.2019.01.170.

(57) Berkdemir, A.; Gutiérrez, H. R.; Botello-Méndez, A. R.; Perea-López, N.; Elías, A. L.; Chia, C. I.; Wang, B.; Crespi, V. H.; López-Urías, F.; Charlier, J. C.; Terrones, H.; Terrones, M. Identification of Individual and Few Layers of WS2 Using Raman Spectroscopy. *Sci. Rep.* **2013**, *3*, 1–8. https://doi.org/10.1038/srep01755.

(58) Liu, J.; Notbohm, J. K.; Carpick, R. W.; Turner, K. T. Method for Characterizing Nanoscale Wear of Atomic Force Microscope Tips. *ACS Nano* **2010**, *4* (7), 3763–3772. https://doi.org/10.1021/nn100246g.

(59) Grierson, D. S.; Liu, J.; Carpick, R. W.; Turner, K. T. Adhesion of Nanoscale Asperities with Power-Law Profiles. *J. Mech. Phys. Solids* **2013**, *61* (2), 597–610. https://doi.org/10.1016/j.jmps.2012.09.003.

(60) Gustavsson, F.; Jacobson, S.; Cavaleiro, A.; Polcar, T. Frictional Behavior of Self-Adaptive Nanostructural Mo-Se-C Coatings in Different Sliding Conditions. *Wear* **2013**, *303* (1–2), 286–296. https://doi.org/10.1016/j.wear.2013.03.032.

(61) Eichfeld, S. M.; Hossain, L.; Lin, Y. C.; Piasecki, A. F.; Kupp, B.; Birdwell, A. G.; Burke, R. A.; Lu, N.; Peng, X.; Li, J.; Azcatl, A.; McDonnell, S.; Wallace, R. M.; Kim, M. J.; Mayer, T. S.; Redwing, J. M.; Robinson, J. A. Highly Scalable, Atomically Thin WSe2grown via Metal-Organic Chemical Vapor Deposition. *ACS Nano* **2015**, *9* (2), 2080–2087. https://doi.org/10.1021/nn5073286.

(62) Wang, S.; Rong, Y.; Fan, Y.; Pacios, M.; Bhaskaran, H.; He, K.; Warner, J. H. Shape Evolution of Monolayer MoS2 Crystals Grown by Chemical Vapor Deposition. *Chem. Mater.* **2014**, *26* (22), 6371–6379. https://doi.org/10.1021/cm5025662.

(63) Schwarz, U. D.; Zwörner, O.; Köster, P.; Wiesendanger, R. Quantitative Analysis of the Frictional Properties of Solid Materials at Low Loads. I. Carbon Compounds. *Phys. Rev. B* **1997**, *56* (11), 6987–6996. https://doi.org/10.1103/PhysRevB.56.6987.

(64) Yang, L.; Tu, Y. S.; Tan, H. L. Influence of Atomic Force Microscope (AFM) Probe Shape on Adhesion Force Measured in Humidity Environment. *Appl. Math. Mech. (English Ed.* **2014**, *35* (5), 567–574. https://doi.org/10.1007/s10483-014-1813-7.

(65) Polcar, T.; Evaristo, M.; Cavaleiro, A. Self-Lubricating W-S-C Nanocomposite Coatings. *Plasma Process. Polym.* **2009**, *6* (6–7), 417–424. https://doi.org/10.1002/ppap.200930005.

(66) Buzio, R.; Boragno, C.; Valbusa, U. Nanotribology of Cluster Assembled Carbon Films. *Wear* **2003**, *254* (10), 981–987. https://doi.org/10.1016/S0043-1648(03)00303-X.

(67) Moser, J.; Levy, F. Crystal Reorientation and Wear Mechanisms in Mos2 Lubricating Thin-Films Investigated By TEM. *J. Mater. Res.* **1993**, *8* (1), 206–213. https://doi.org/10.1557/jmr.1993.0206.

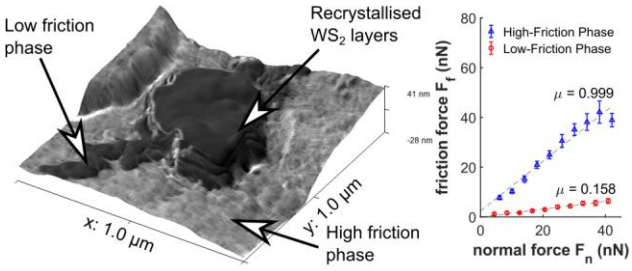

For Table of Contents Only